A STRESS BASED CRITICAL-PLANE APPROACH FOR STUDY OF ROLLING CONTACT FATIGUE CRACK PROPAGATION IN PLANET GEARS

P. Depouhon*, C. Sola, B. Descharrières, A. Delabie
*pierre.depouhon@airbus.com
Airbus, Aéroport international Marseille Provence, 13725 Marignane, France

Abstract

This paper presents a contribution to the study of rolling contact fatigue (RCF) in the specific case of a planet gear containing an integrated bearing. Propagation of micro-cracks starting from the bearing race surface and leading to spalling is a typical damage mode of these components. However, in some specific cases, cracks can bifurcate into the core, leading to the complete failure of the component. Based on experimental observations, discussion on the interactions between spalling and in-core cracks suggests a competition between the two phenomena. In order to understand the main drivers of crack propagation, a stress based critical-plane approach is developed and confronted to crack observations. It enables to highlight that several factors, such as the contact pressure at the roller/race interface, the rim ovalization, and residual stresses due to a thermochemical treatment, play a major role on the crack behavior.

1. INTRODUCTION

Propagation of cracks in rolling contact fatigue (RCF) is a common damage phenomenon in bearings and gears. Generally, the RCF cracks initiate on the contact surface and remain located close to it [1]. The presence of numerous micro cracks leads to the release of metal particles (micro-pitting). Over time, the size of the released particles and the depth of cracks increase, leading to spalling phenomena. One or several cracks can thus bifurcate into the core and lead to the complete failure of the component.

In helicopter drive systems, these kinds of consequences are usually avoided by the detection of metal particles released during spalling and transported by the lubricating oil up to the detection system. Nevertheless, the spalling rate and the subsurface crack path can be significantly dispersive [2, 3] in such a way that it makes difficult the accurate evaluation of the margin. Main drivers and potential interactions between spalling and in-core cracks have thus to be better understood and mastered.

There has been considerable research devoted to the area of surface and subsurface crack initiation in RCF [1, 2, 4]. Several authors developed initiation criteria based on short crack theory [5], others have modeled the microstructure and simulated the micro cracks propagation at the grain boundaries in order to link contact conditions and material characteristics to the crack initiation threshold [6].
Several experimental [7, 8] and theoretical studies are available on spalling after initiation. Theoretical approaches focused on the simulation of a single crack, in 2D and more recently in 3D, starting from the surface and submitted to the cyclic contact pressure without structural stresses. These detailed models attempt to describe elementary mechanisms such as fluid pressurization, friction, etc. which drive the crack propagation at the very beginning of the crack history, before the release of particles.
Mainly supported by railway industries, other approaches attempt to simulate any 3D RCF crack propagating in the core of the component (rails), involving advanced numerical methods [9].
Thorough work still needs to be done to have predictive simulation of spalling rate and in-core cracks, but research on initiation, spalling and subsurface crack propagation already enables to understand the main drivers of these damage modes.
This paper presents a contribution to the understanding of in-core RCF crack propagation in the particular case of a planet gear outer ring, a component of a main gear box epicyclical module. It proposes to identify, through a multiaxial stress analysis, the main drivers of the crack propagation. The multiaxial stress analysis is based on critical plane approaches, widely used for the definition of multiaxial fatigue criteria [10]. Without simulating the crack, the model attempts to define stress fields representative of the crack behavior. They are established from the confrontation between the theoretical stress tensor and the experimental RCF cracks in the outer ring of a planet gear.

2. SPALLING AND CRACK OBSERVATION

2.1. Standard spalling behavior

In bearings, propagation of micro cracks under cyclic loading (due to the contact pressure at the roller/race interface) is the origin of micro pitting and spalling (Fig. 1). Considering the high metallurgical quality of modern bearing steels, cracks generally initiate from surface defects rather than from subsurface ones. A main crack then propagates at a shallow angle and bifurcates as a secondary crack returning to the surface and releasing a metal particle.

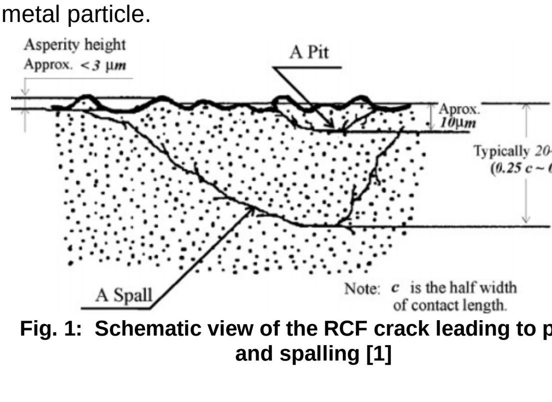

Fig. 1: Schematic view of the RCF crack leading to pitting and spalling [1]

Otherwise, it is well established that lubrication conditions play a major role on the crack behavior (Fig. 2). Indeed, the oil film protects the surface, reduces wear, and in case of crack initiation, fluid pressurization at the crack front accelerates subsurface crack favoring in-core propagation. Case (L3) in Fig. 2 well represents the kind of crack behavior met in the planet gear as presented in the next section.

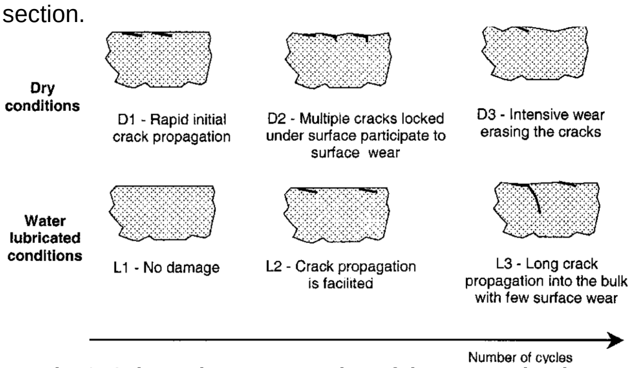

Fig. 2: Schematic representation of damage under dry conditions and water lubrication under RCF [11].

2.2. Particular case of subsurface crack in a planet gear

The studied planet gear is a pinion containing an integrated spherical bearing constituted of 2 rows of rollers (Fig. 3). The outer ring, made of carburized steel, is thus submitted to complex loadings, but micro-pitting and spalling on inner and outer races remain the most frequent types of in-service damage.

Fig. 3: Studied planet gear

Usually, cracks remain located close to the race surface and release particles until detection. However, a different crack behavior can occur when only a few particles are released. This is the case study detailed here after.

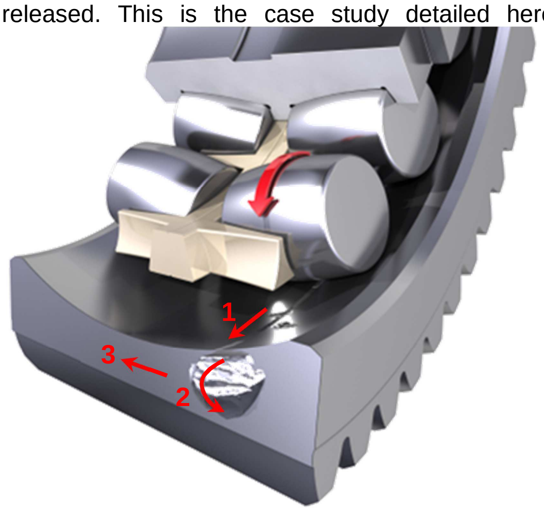

Fig. 4: Schematic view of the damaged outer ring

Fig. 4 presents a schematic overview of the studied outer ring. Fig. 5 shows different views of the crack, from micro pitting initiation, to development in spalling and in long subsurface crack propagation until opening of the outer ring.

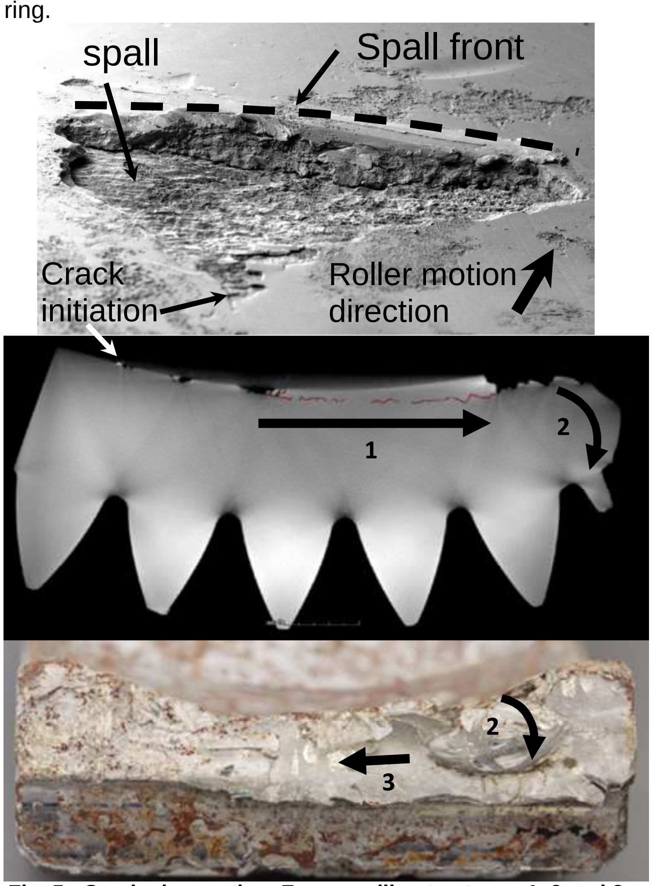

Fig. 5 : Crack observation. From spalling to stages 1, 2 and 3 of crack propagation.

The evolution of the subsurface crack propagation is divided into three main stages. The first one is characterized by propagation in the carburized layer, almost parallel to the race surface but slightly inclined in the direction of the core. Fig. 6 focuses on this first stage of propagation. The crack network looks very structured. It is constituted of a main crack, almost parallel to the surface and of many secondary branches returning to the surface but self-arrested before reaching it.

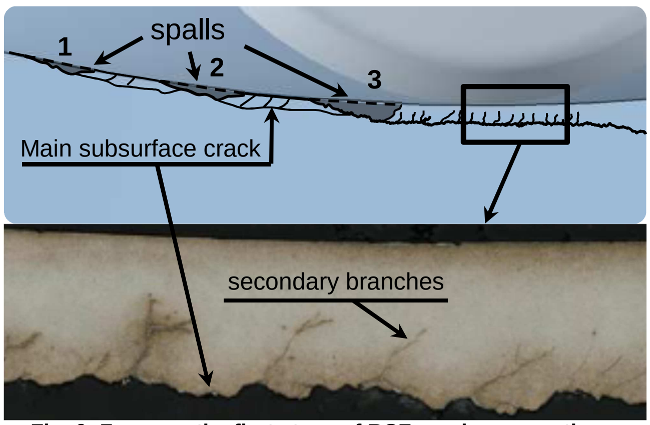

Fig. 6: Zoom on the first stage of RCF crack propagation

Indeed, metallurgical investigations have demonstrated that these secondary branches were fatigue cracks. Striation counting in these branches, close to their crack front has shown that the crack growth rate is very close to the propagation threshold. Furthermore, a detailed analysis of the 3 spalls (Fig. 6) indicates that spall 1 is the origin of the main crack.
The development of spalls could be influenced by the presence of the main subsurface crack. It also can be driven by the local overpressure due to the edge effect at the spall front (Fig. 5). Thus, the mechanism of release particles (spalling rate) is not directly driven by the main subsurface crack.
On the other hand, the evolution of the subsurface crack seems highly dependent on the spalling rate. Indeed, it is well established that cyclic Hertzian stress due to the contact pressure (enhanced by oil pressurization) is the driver of such subsurface propagation. If particles are not released, they still transmit Hertzian stresses to the crack front, favoring its propagation. If they are released close to the main crack front, it becomes unloaded and can be arrested. Thus, one can see a competition between the spalling rate and the subsurface crack growth rate.

The second stage (stage 2 on Fig. 4 and Fig. 5) of the crack propagation starts when the main crack reaches the end of the carburized layer. It corresponds to the bifurcation of the main crack into the core which is characterized by a double curvature (ellipsoidal shape) crack path.

The third stage (stage 3 on Fig. 4 and Fig. 5) is characterized by an almost coplanar propagation mainly oriented in axial direction until complete opening of the outer ring.

3. INTERNAL STRESS IN OUTER RING

In order to understand the drivers of these 3 stages of propagation, a stress analysis was performed. First, the total stress tensor in the outer ring was computed. Secondly, a critical plane analysis of this total stress was developed and confronted to crack observations.
The outer ring is submitted to 3 main sources of stress, the so called "ovalization", "hertzian" and "residual" stresses.
Due to the complexity of the total loading, the stress analysis was performed at each depth of the rim, only under the line of maximum contact pressure (Fig. 7).

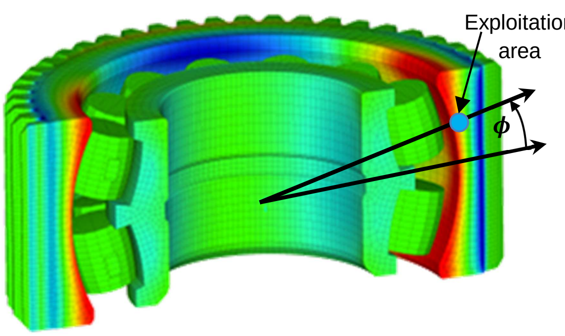

Fig. 7: Area of stress exploitation

3.1. "Ovalization" stress

The ovalization stress corresponds to the distortion of the outer rim under the global loads transmitted by the gear teeth and the crankpin (Fig. 8). A static FEM computation of the planet gear was performed to obtain the ovalization stress tensor in the rim. This stress field is locally comparable to an alternate bending state.

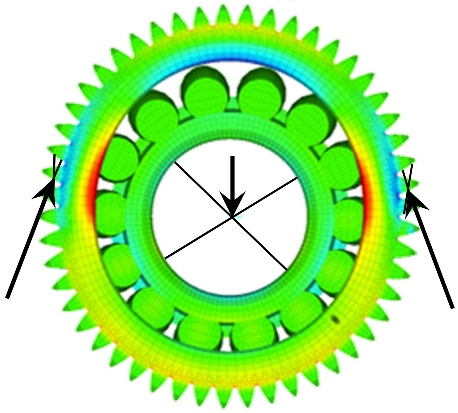

Fig. 8: Rim ovalization under global loads. Hoop stress is represented.

3.2. "Hertzian" stress

The load repartition on each roller was obtained through the FEM of the planet gear. The hertzian stress tensor in the rim was analytically expressed thanks to the theory of potentials [12] under the following assumptions: the contact area is elliptic, the contact pressure distribution is also elliptic and the rim can be assimilated to a semi-infinite body compared to the size of the contact area (Fig 9).

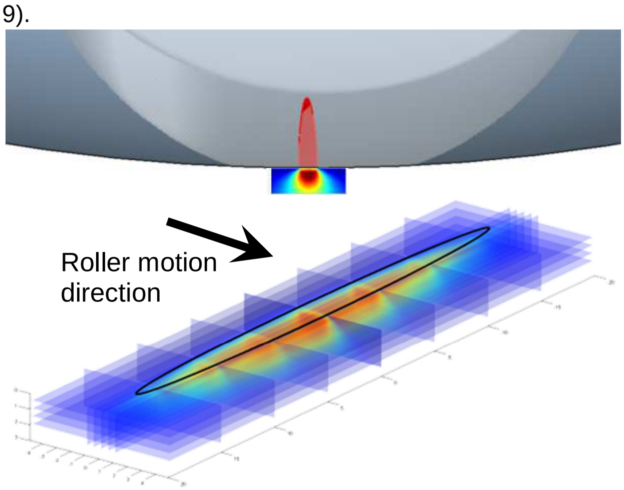

Fig 9 : Hertzian stress fields under elliptical pressure distribution and elliptical contact area (Von Mises).

3.3. Residual stress

Unlike ovalization and hertzian stresses which impose a cyclic loading to the material, the residual stresses due to the carburizing process generate a static state of stress. Thus, if they are not responsible for the crack propagation, they can play a major role on the crack behavior (growth rate and orientation). Because it is localized in the very vicinity (≈20µm) of the surface, the high level of compressive residual stress due to the grinding process is neglected in comparison to the one generated by carburizing, much deeper and influent in the core of the rim.

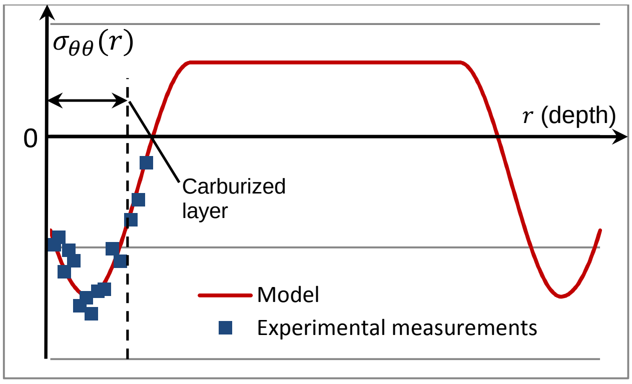

Fig. 10: Identification of the simplified residual stress model from experimental data obtained by X-ray diffraction

The source of residual stresses due to carburizing involves complex phenomena such as phase transformations which were not modeled in this work. To obtain an order of magnitude of the residual stress level, the eigenstrain method was used [13]. The eigenstrain is assumed to be purely hydrostatic and localized in the carburized layer. It is identified through experimental in-depth residual stress profiles obtained by X-ray diffraction on the outer race (Fig. 10). To simplify the identification process, residual stresses in the rim are considered well represented by residual stresses in an infinite plate of thickness equal to the radial distance between the tooth foot and the point of residual stress measurement on the outer race. In this case, the analytic relation between residual stresses and the eigenstrain, expressed in the spherical frame defined in Fig. 11, is as follows:

(1) $$\sigma_{\theta\theta}(r) = \sigma_{\phi\phi}(r) = \frac{E}{1-\nu}(a\,r + b - \varepsilon_L(r))$$

with

$$\begin{cases} a = \dfrac{6}{H^2}\left(\dfrac{2}{H}\displaystyle\int_0^H r\,\varepsilon_L(r)dr - \int_0^H \varepsilon_L(r)\,dr\right) \\ b = \dfrac{6}{H^2}\left(\dfrac{2H}{3}\displaystyle\int_0^H \varepsilon_L(r)dr - \int_0^H r\,\varepsilon_L(r)\,dr\right) \end{cases}$$

E and ν are Young's modulus and Poisson's coefficient. As a first approximation both are considered constants in the depth. Then, constants a and b only depend on the rim thickness H and on the eigenstrain in-depth profile $\varepsilon_L(r)$.

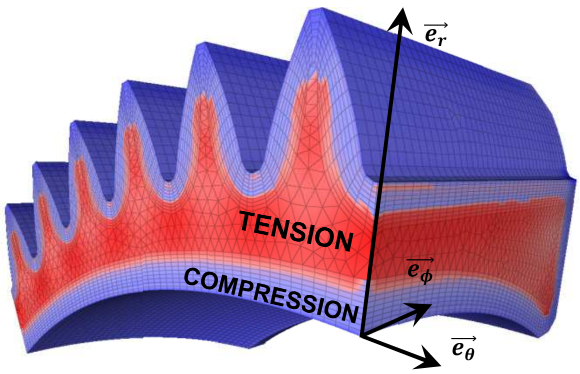

Fig. 11: Signed Von Mises stress field of simulated residual stresses due to the carburizing

Their expressions are deduced from the global equilibrium of the plate. The identification process is to find $\varepsilon_L(r)$ that minimize the discrepancy between the modeled stress profile and X-ray diffraction measurements in the least-squares sense. Fig. 10 shows the results of this identification.

Available experimental stress data only indicate a compressive state of stress located in the carburized layer, whereas the theoretical stress field is known at each depth and gives information beyond the treated layer. It shows that the core of the rim is submitted to a tensile state of stress to balance the compression of the carburized layers.

Fig. 11 presents a 3D finite element simulation of the residual stresses in the outer ring. The previously identified eigenstrain was introduced through an equivalent thermal simulation [13]. This view highlights the tension and compression areas which roughly represent the carburized layer (in blue), reached by diffusion of carbon during carburizing, and the in-core material (in red), not enriched in carbon. This simulation also enables to define the validity domain of the plate hypothesis used for eigenstrain identification. For computational time efficiency reasons, the plate model was retained for the critical plane analysis.

3.4. Total stress tensor computation

The total deformation of the outer ring can be considered small, such that no geometric non linearity has to be taken into account. Furthermore, the material behavior is elastic and remains loaded in its elastic domain, and residual stresses are not significantly affected by cyclic hertzian stresses.

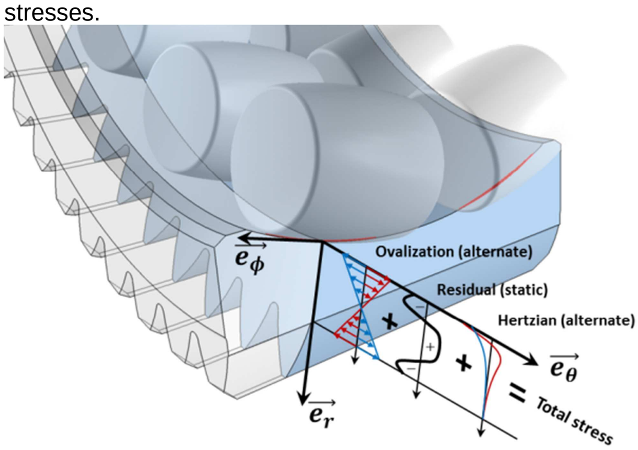

Fig. 12: Schematic summation of stresses in the depth under the line of maximum contact pressure

Thus, the total stress tensor can be simply expressed as the sum of the 3 stress contributions (Eq. 2), that are schematically represented in the rim depth (r) under the line of max contact pressure (a given ϕ_m) on Fig. 12.

(2) $$\sigma(r,t) = \sigma_{tot}(r,\theta,\phi_m) = \sum_{i=\{ov;res;her\}} \sigma_i\,(r,\theta,\phi_m)$$

The variable θ is assimilated to the time t, such as at each depth r under contact, the loading path is entirely defined by the total stress tensor $\sigma(r,t)$.

4. CRITICAL PLANE ANALYSIS

4.1. Principle

The critical plane analysis is widely used for the definition of multiaxial fatigue criteria [10]. It consists in the analysis of the stress cycle on an arbitrary fixed material plane. Whatever their complexity (multiaxial and non-proportional stress loading path), all states of stress in a given material plane can be decomposed into a shear and a tension-compression contributions. In metals, fatigue cracks are known to start in mode II by sliding in some unfavorably oriented grains. Thus, fatigue criteria based on the critical plane approach postulate that the crack initiation will occur in the plane which maximizes the alternate shear or an equivalent stress [10].
In the case of the planet gear outer ring, due to hertzian contribution, the RCF loading path is found highly triaxial and non-proportional, which indicates that cracks propagate under complex mixed-mode conditions. The critical plane analysis is thus performed to study the potential dominant propagation mode at a given depth under contact.

Using a critical plane analysis to study the crack behavior without simulating it is questionable. Indeed, it implicitly assumes that the stress field is not modified by the presence of the crack, and that the final crack path is not affected by history effects. These hypotheses are obviously experimentally invalidated, which justifies the effort provided by many authors to correctly predict the path of a crack loaded in mixed mode conditions. However, the aim of this study was to provide a tool favoring the understanding of RCF cracks drivers in planet gears. Despite its inability to predict the good orientation of critical planes at the crack front, this thorough analysis of the stress tensor provides some useful information on these drivers, which has been partly confirmed by experimental observations. This approach also facilitates the comparison of different planet gears regarding their RCF behavior.

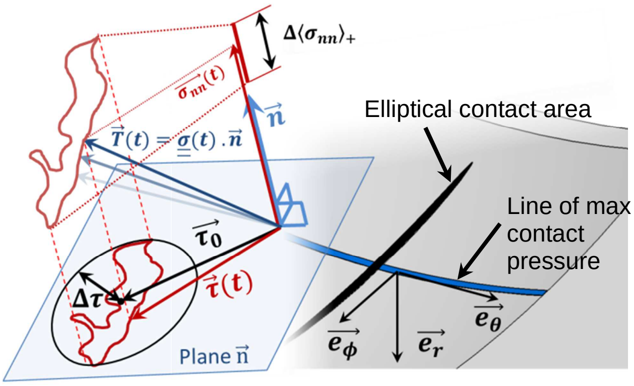

Fig. 13: From total stress tensor to mode I and II critical plane analysis at a given depth under contact

The analysis was performed on both I and II propagation modes. $\Delta\langle\sigma_{nn}\rangle_{+,crit}$ and $\Delta\tau_{crit}$ are respectively the critical alternate normal stress which represent the mode I crack growth rate driver and the critical alternate shear stress which corresponds to the mode II crack growth rate driver. Fig. 13 shows the critical plane analysis process and illustrates the relation between the total stress tensor and the stress fields assumed to be the drivers of mode I and II crack propagation growth rates.

At each depth under the line of maximum contact pressure, the stress vector $\vec{T}(t) = \sigma(t)\,\vec{n}$ is computed. $\sigma(t)$ is the total stress tensor whereas $\vec{n}$, defined in the spherical frame, is the normal to a given material plane. To perform the mode II analysis, $\vec{T}(t)$ is then projected on the plane to obtain the shear stress $\vec{\tau}(t)$. In multiaxial loading, a way of defining the amplitude of $\vec{\tau}(t)$ is to find the radius of the smaller circle circumscribed to the $\vec{\tau}(t)$ loading path. The radius $\Delta\tau$ is thus defined as the amplitude of the shear stress and the center $\vec{\tau_0}$ corresponds to its mean part. Once $\Delta\tau$ is known, the same analysis is performed on all possible planes and the critical alternate shear acting on the so called mode II critical plane is defined, at a given depth, by:

$$\Delta\tau_{crit}(r) = \max_{\vec{n}} \Delta\tau(r, \vec{n}) \quad (3)$$

To perform the mode I analysis, $\vec{T}(t)$ is projected on the normal vector. Considering that a negative normal stress (compression state) does not have an influence on the mode I crack propagation, only the positive part of the normal stress $\langle\sigma_{nn}\rangle_+$ is taken into account. The amplitude of the normal stress is thus $\Delta\langle\sigma_{nn}\rangle_+ = \max\langle\sigma_{nn}\rangle_+ - \min\langle\sigma_{nn}\rangle_+$. As for mode II analysis, all planes are studied and the critical normal stress is defined, at a given depth, by:

$$\Delta\langle\sigma_{nn}\rangle_{+,crit}(r) = \max_{\vec{n}} \Delta\langle\sigma_{nn}\rangle_+(r, \vec{n}) \quad (4)$$

4.2. Mode I analysis : Alternate normal stress

Fig. 14 presents the in-depth profiles of the alternate critical normal stress, alternate hoop stress and residual stress under the line of maximum contact pressure.

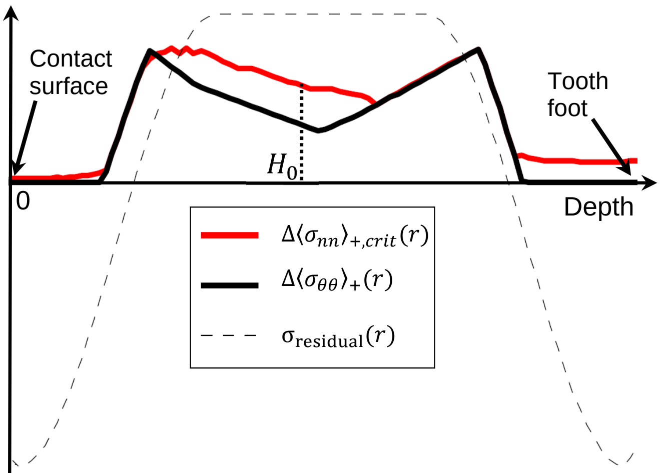

Fig. 14: In-depth alternate normal stresses and residual stress profiles under the line of maximum contact pressure

The alternate hoop stress was taken as a reference. Indeed, in the step 3 of crack propagation (Fig. 5), the crack front is approximatively contained in the plane $(\vec{e_\phi}, \vec{e_r})$ (Fig. 12), which suggests that, if a crack propagates in mode I, the alternate hoop stress $\Delta\langle\sigma_{\theta\theta}\rangle_+$ (in $\vec{e_\theta}$ direction) should drive it. Results presented on Fig. 14 indicate that there is a significant level of alternate hoop stress $\Delta\langle\sigma_{\theta\theta}\rangle_+$ due to the rim ovalization, which confirms that the step 3 of crack evolution is compatible with a mode I propagation. Fig. 14 also shows that due to a compressive state of residual stresses, $\Delta\langle\sigma_{\theta\theta}\rangle_+$ and $\Delta\langle\sigma_{nn}\rangle_{+,crit}$ are null or negligible in the carburized layer. Thus, whatever the considered material plane, it means that there is no evidence of mode I crack propagation due to structural stresses in the carburized layer. The mode II critical plane analysis presented in the next section highlights, in accordance with the literature [11], that the crack is more likely to propagate in mode II in the carburized layer. The alternate normal stress then enables to define the existence areas of mode I and mode II crack propagation, which are illustrated on Fig. 15.

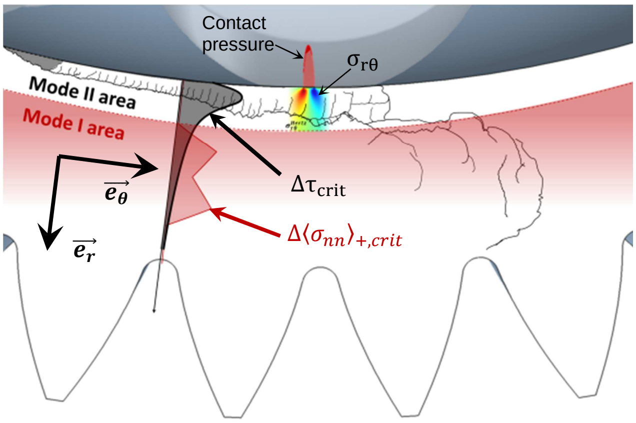

Fig. 15 : Areas of existence of mode I and mode II crack propagation

An interesting result is exposed on Fig. 15, which superimposes the areas of existence of the propagation modes with the crack path. The beginning of the crack bifurcation is located at the interface between mode I and mode II, when the residual stress becomes positive. The crack behavior seems significantly different, depending on the dominant propagation mode. The almost "coplanar" propagation of the main crack with numerous small branches in the carburized layer becomes a network of "curved" cracks in "C" shape in the core of the rim.
The main "C" crack on the right of Fig. 15 corresponds to the step 2 of crack propagation. In 3D, the "C" crack rather follows an ellipsoidal surface shape, centered under the line of max contact pressure (Fig. 5). The mode I analysis indicates that both step 2 and step 3 are compatible with the mode I dominated propagation. However, the crack behavior seems very different between these two steps. Whereas step 3 is clearly driven by ovalization stresses, the complexity of the crack path in step 2 indicates that it is certainly driven by another source of stress.

Analysis of $\boldsymbol{\Delta\langle\sigma_{nn}\rangle_{+,crit}}$ on Fig. 14 enables to partly understand the driver of the step 2 crack propagation. Indeed, the comparison between $\boldsymbol{\Delta\langle\sigma_{\theta\theta}\rangle_+}$ and $\boldsymbol{\Delta\langle\sigma_{nn}\rangle_{+,crit}}$ shows that from the end of the carburized layer up to a certain depth $\boldsymbol{\Delta\langle\sigma_{nn}\rangle_{+,crit}} > \boldsymbol{\Delta\langle\sigma_{\theta\theta}\rangle_+}$. It means that in this depth range, the mode I critical plane is not oriented by $\overrightarrow{\boldsymbol{e_\theta}}$. A detailed analysis of the mode I critical plane orientation and of the stress cycle at the depth $\boldsymbol{H_0}$ under the contact (Fig. 14) is presented on Fig. 16, Fig. 17 and Fig. 18. At the depth $\mathbf{H_0}$, for each computed plane of normal $\vec{\mathbf{n}}$, the coordinates of the alternate normal stress vector $\overrightarrow{\mathbf{\Delta T_n}} = \mathbf{\Delta\langle\sigma_{nn}\rangle_+}\,\vec{\mathbf{n}}$ are plotted in the spherical frame. This gives the following envelop of the alternate normal stresses (Fig. 16), which gives an information on both the amplitude and the orientation of normal stresses, and thus of the mode I critical plane.

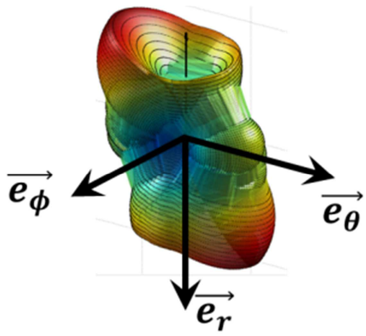

Fig. 16: Envelope of alternate normal stress $\Delta\langle\sigma_{nn}\rangle_+$ beyond the carburized layer, at the H_0 depth (see Fig. 14)

The envelope presented on Fig. 16 indicates that there is almost no mode I loading in the $\overrightarrow{e_\phi}$ direction under the line of maximum contact pressure. The normal to mode I critical plane is thus contained in the plane $(\overrightarrow{e_r}, \overrightarrow{e_\theta})$. Thus the problem, which can be reduced in two dimensions, is represented on Fig. 17.

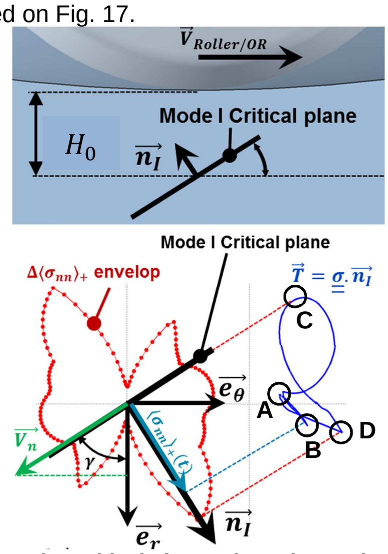

Fig. 17 : Mode I critical plane orientation at the H_0 depth

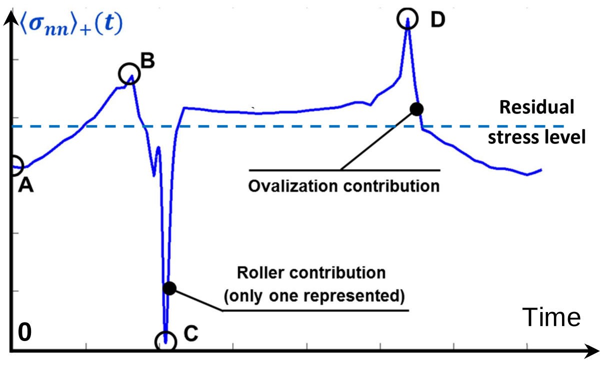

Fig. 18 : Normal stress loading path on the mode I critical plane at the H_0 depth under the line of maximum contact pressure

Fig. 17 shows the envelope of $\Delta\langle\sigma_{nn}\rangle_+$ in the plane $(\overrightarrow{e_r}, \overrightarrow{e_\theta})$. The mode I critical plane is defined by its normal $\overrightarrow{n_I}$ oriented by an angle γ with respect to $\overrightarrow{\boldsymbol{e_\theta}}$. The loading path

of the stress vector $\vec{T}$ applied on this plane is also represented. Its projection on $\overrightarrow{n_I}$ in respect to time gives the normal stress $\langle\sigma_{nn}\rangle_+$(t) presented on Fig. 18. Characteristic points A, B, C, D are plotted on both Fig. 17 and Fig. 18. They correspond to different times in the stress cycle. The plane oriented by $\overrightarrow{e_\theta}$ maximizes the ovalization effect, which increases the distance between A and D. It also reduces the hertzian contribution in such a way that $\Delta\langle\sigma_{\theta\theta}\rangle_+ = \sigma_D - \sigma_A$. On the contrary, the critical plane oriented by $\overrightarrow{n_I}$ is submitted to a significant hertzian contribution such as $\Delta\langle\sigma_{nn}\rangle_+ = \sigma_D - \sigma_C$. This result indicates that a crack contained in this plane is initially opened by the static tensile residual stress and cyclically closed when the roller passes over it, in such a way that the crack propagates faster under this loading than under the ovalization one. Otherwise, point C almost returns to zero, which means that the critical plane is the one which maximizes the hertzian contribution. Indeed, if point C is negative, the negative part of the signal would not contribute to crack propagation whereas if it were positive, the signal amplitude would not be maximized. The tensile residual stress thus seems to play a major role on crack propagation in allowing cyclic hertzian stresses to generate a mode I crack propagation.
Moreover, if the ovalization stress cycle (points D, A, B on Fig. 17) does not involve alternate shear in the mode I critical plane, this is not the case in the cyclic hertzian contribution (points B, C, D on Fig. 17), for which the projection of $\vec{T}$ on the critical plane induces an alternate shear in the same order of magnitude as for the alternate normal stress. Thus, if the crack propagation due to the hertzian stress seems to be mode I dominated, the loading path rather suggests a non-proportional mixed mode I + II propagation which could be a contributing factor to the complexity of the step 2 cracks shape.
The hypothesis of a propagation driven by the hertzian contribution in the tensile state of residual stress is reinforced by the crack observation on Fig. 5. Indeed, the ellipsoidal shape of the crack path is centered under the line of maximum contact pressure and only located in the hertzian influenced area.

4.3. Mode II analysis : alternate shear stress

Due to both residual and hertzian contributions, mode I analysis has confirmed a triaxial compressive state of stress in the carburized layer, which prevents a mode I propagation. The study then focuses on the mode II potential drivers on crack propagation. Fig. 19 presents $\Delta\tau_{\text{crit}}$ and $\Delta\langle\sigma_{nn}\rangle_{+,crit}$ in-depth profiles.

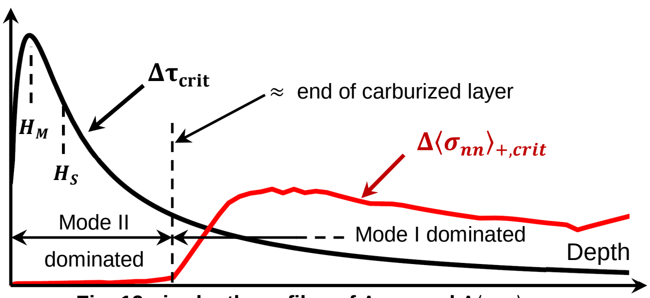

Fig. 19 : in-depth profiles of $\Delta\tau_{\text{crit}}$ and $\Delta\langle\sigma_{nn}\rangle_{+,crit}$

It shows that the carburized layer is submitted to a significant level of alternate shear due to cyclic hertzian stresses which let suppose that the crack is driven by a mode II loading in the carburized layer. Fluid pressurization effects highlighted by several authors [14] were not modeled in this work. However, they are known to play a major role on the crack growth rate. As a consequence, the crack front is not only driven by mode II but is rather submitted to a sequential mode I and mode II. Nevertheless, the mode I loading due to fluid pressurization which depends on the contact pressure and on the oil viscosity, can be viewed as a growth rate “catalyst” of a crack fundamentally driven by the mode II loading [14,15]. This point of view is compatible with a confrontation between the step 1 crack observation (Fig. 5 and Fig. 6) and the mode II critical plane orientations (Fig. 20).

The orientation of alternate shear can be known through the analysis of its envelope. At the depth of maximum alternate shear $\boldsymbol{H_M}$, for each computed plane of normal $\vec{\boldsymbol{n}}$, the coordinates of the vector $\vec{\boldsymbol{\tau}}(\boldsymbol{t}) - \overrightarrow{\boldsymbol{\tau_0}}$ are plotted in the spherical frame, and give the envelope of the alternate shear presented on Fig. 20.

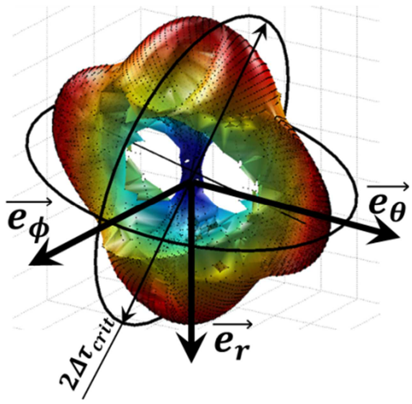

Fig. 20 : Envelope of alternate shear stress $\Delta\tau$ at the H_M depth (Fig. 19**)**

As for mode I analysis, alternate shear envelope indicates that there is almost no mode II loading in the $\overrightarrow{e_\phi}$ direction whereas $\overrightarrow{e_r}$ and $\overrightarrow{e_\theta}$ are preferential shear directions. The symmetry of the stress tensor involves the presence of 2 mode II critical planes at 90° from each other. When no friction is considered at the roller/race interface, mode II critical planes are strictly parallel and perpendicular to the race (which means that $\Delta\tau_{\text{crit}} = \Delta\sigma_{r\theta}$ where $\sigma_{r\theta}$ is illustrated on Fig. 15). In step 1 of the propagation (Fig. 5 and Fig. 6), spalls and subsurface cracks seem compatible with these planes. Indeed, the main crack is almost coplanar and parallel to the surface, and the secondary branches are globally perpendicular to both the surface and the rolling direction ($\overrightarrow{e_\theta}$). However, the envelope on Fig. 20 shows a multiplicity of preferential shear directions around critical planes, which means that the crack orientation can be significantly influenced by microstructure heterogeneities (grain boundary, etc.).

It appears from these considerations that the alternate shear due to hertzian cyclic stresses seems to be the main driver of the damage in the carburized layer. The spalling rate can thus be indirectly related to the level of $\Delta\tau_{\text{crit}}$ from the race surface to a depth H_S, corresponding to the experimental maximum spalling depth, and the subsurface crack growth rate can be related to the level of $\Delta\tau_{\text{crit}}$ between H_S and the carburized layer thickness.

5. CONCLUSION

The case of a planet gear subjected to a spalling damage leading to an in-core crack presence has been studied. Based on cracks and spalls observations, discussion on the interaction between spalling and subsurface crack suggested a competition between the two phenomena.

In order to improve the understanding of the parameters driving the fatigue cracks, a stress based critical-plane approach was performed on the outer ring of the planet gear. The analysis enabled to draw the following conclusions:

- The first step of the subsurface propagation and the spalling rate are both driven by the contact pressure.
- The second step is driven by the contact pressure coupled with residual stresses generated by thermochemical treatment
- The third step is driven by the rim ovalization

The definition of two alternate stress fields considered as representative of the crack growth rate enables to identify the design parameters influencing the crack propagation. It thus facilitates the sizing of planet gears.

However, thorough work still needs to be carried out to better understand the influential parameters on the mechanisms of release particles and on the in-core crack occurrence conditions. A better understanding of the dispersive nature of the involved phenomena will also be necessary to improve the sizing of planet gears and more generally, of integrated bearings submitted to significant structural stresses.

References

[1] Y. Ding and N. F. Rieger, “Spalling formation mechanism for gears,” *Wear*, vol. 254, no. 12, pp. 1307–1317, Nov. 2003.

[2] F. Sadeghi, B. Jalalahmadi, T. S. Slack, N. Raje, and N. K. Arakere, “A Review of Rolling Contact Fatigue,” J. Tribol., vol. 131, no. 4, p. 041403, 2009.

[3] L. Rosado, N.H. Forster, K.L. Thompson, and J.W. Cooke, “Rolling contact fatigue life and spall propagation of AISI M50, M50NiL, and AISI 52100, Part I: experimental results”, Tribology Transactions, 53(1), 29-41, 2009.

[4] C. Santus, M. Beghini, I. Bartilotta, and M. Facchini, “Surface and subsurface rolling contact fatigue characteristic depths and proposal of stress indexes,” Int. J. Fatigue, vol. 45, pp. 71–81, Dec. 2012.

[5]J. W. Ringsberg and A. Bergkvist, “On propagation of short rolling contact fatigue cracks,” *Fatigue & Fracture of Engineering Materials & Structures*, vol. 26, no. 10, pp. 969–983, 2003.

[6] R. V. Pulikollu,N. Bolander, T. Shen, S. Vijayakar,M. D. Spies, “Microstructure-based fatigue life prediction tool for rotorcraft spiral bevel gears,” in *AHS* International Forum 69, 2013.

[7] J.-W. Seo, S.-J. Kwon, D.-H. Lee, and H.-Y. Choi, “Analysis of contact fatigue crack growth using twin-disc tests and numerical evaluations,” *International Journal of Fatigue*, vol. 55, pp. 54–63, Oct. 2013.

[8] M. Dallago, M. Benedetti, S. Ancellotti, and V. Fontanari, “The role of lubricating fluid pressurization and entrapment on the path of inclined edge cracks originated under rolling–sliding contact fatigue: Numerical analyses vs. experimental evidences,” *Int. J. Fatigue*, vol. 92, pp. 517–530, Nov. 2016.

[9] S. Bogdański and P. Lewicki, “3D model of liquid entrapment mechanism for rolling contact fatigue cracks in rails,” *Wear*, vol. 265, no. 9–10, pp. 1356–1362, Oct. 2008.

[10] Dang Van K, Cailletaud G, Flavenot JF, Le Douaron A and Lieurade HP, “Criterion for high cycle fatigue failure under multiaxial loading,” *Biaxial and multiaxial fatigue*, EGF 3, pp. 459–78, 1989.

[11] M. C. Dubourg and V. Lamacq, “A Predictive Rolling Contact Fatigue Crack Growth Model: Onset of Branching, Direction, and Growth—Role of Dry and Lubricated Conditions on Crack Patterns,” *Journal of Tribology*, vol. 124, no. 4, p. 680, 2002.

[12] D. A. Hills, D. Nowell and A. Sackfield, *Mechanics of elastic contacts,* Butterworth–Heinemann, Oxford, 1993.

[13] P. Depouhon, J.-M. Sprauel, M. Mailhé, E. Mermoz, “Modeling of distortions induced by the nitriding process,” *Mechanics & Industry*, vol. 16, n0. 107, 2015.

[14] S. Ancellotti, M. Benedetti, M. Dallago, and V. Fontanari, “Fluid Pressurization and Entrapment Effects on the SIFs of Cracks produced under lubricated Rolling-Sliding Contact Fatigue,” *Procedia Structural Integrity*, vol. 2, pp. 3098–3108, 2016.

[15] V. Doquet and G. Bertolino, “Local approach to fatigue cracks bifurcation,” *International Journal of Fatigue*, vol. 30, no. 5, pp. 942–950, May 2008.